Correspondence to:
J. Bapst,
jnbapst@lpl.arizona.edu

Thermophysical Properties of the North Polar Residual Cap using Mars Global Surveyor Thermal Emission Spectrometer

J. Bapst[1,2] , S. Byrne[1] , J. L. Bandfield[3] , and P. O. Hayne[4]

[1]Lunar and Planetary Laboratory, University of Arizona, Tucson, AZ, USA, [2]Now at Jet Propulsion Laboratory, California Institute of Technology, Pasadena, CA, USA, [3]Space Science Institute, Boulder, CO, USA, [4]Astrophysical and Planetary Sciences, University of Colorado Boulder, Boulder, CO, USA

Abstract Using derived temperatures from thermal-infrared instruments aboard orbiting spacecraft, we constrain the thermophysical properties, in the upper few meters, of the north polar residual cap of Mars. In line with previous authors we test a homogeneous thermal model (i.e., depth-independent thermal properties), simulating water ice of varying porosity against observed temperatures. We find that high thermal inertia (>1,000 J m^{-2} K^{-1} s$^{1/2}$ or <40% porosity) provides the best fit for most of the residual cap. Additionally, we test the observed data against models with depth-dependent thermal properties. Models tested converge on similar solutions: we find extensive regions of low surface thermal inertia consistent with a porous layer at the surface (>40% porosity) that densifies with depth into a zero-porosity ice layer at shallow depths (<0.5 m). We interpret this as evidence of recent water ice accumulation. Our results along the edge of the residual cap imply that denser (<40% porosity) ice is present at the surface and coincides with lower albedo. These results suggest that older ice is undergoing exhumation along much of the residual cap margin. The results support recent water ice accumulation having occurred over specific regions, while ablation dominates in others.

Plain Language Summary The polar regions of Mars host kilometer-thick stacks of water ice that have been built up over millions of years. At the north pole today, the top of this ice deposit is interacting with the Martian atmosphere. Whether or not ice at the surface is fluffy (like snow) or dense (like an ice slab) can provide useful information about the polar ice cap and recent climate. Multiple years of surface temperature measurements have been acquired by instruments aboard spacecraft in orbit around Mars. By comparing these values with temperature simulations, we can narrow down the type of ice near the surface. Our results show that the type of ice varies across the polar cap. Some regions appear to be a snow-like surface where the polar cap may be growing. Other regions, most notably along the edge of the polar cap, show denser ice that is likely older. The nature of the ice tells us about the current climate and how these kilometer-thick ice deposits form.

1. Introduction

The north and south polar regions of Mars host polar layered deposits (NPLD and SPLD, respectively) that are sequences of water ice with varying degrees of dust (sufficient to produce visible layering in exposures) and are up to 2- to 3-km thick. Together, they account for the majority of known water ice on Mars (Byrne, 2009; Phillips et al., 2008; Plaut et al., 2007). The spatial extent of the layered deposits is substantial, with the NPLD extending equatorward from the pole at all longitudes to roughly 80°N and the SPLD extending equatorward at some longitudes to 72°S.

The PLDs are thought to have formed over the recent geologic past (10^6–10^8 years; Byrne, 2009; Greve et al., 2010; Herkenhoff & Plaut, 2000; Hvidberg et al., 2012; Levrard et al., 2007; Phillips et al., 2008; Smith et al., 2016), where climate change is driven by changes in orbital elements (Laskar et al., 2004). Due to the abundance of troughs that expose sequences of the layered deposits, the NPLD have been the primary focus for determining a climatological record. Previous studies have explored linking stratigraphic sequences to changes in Martian orbital elements (Becerra et al., 2016; Hvidberg et al., 2012; Laskar et al., 2002; Milkovich & Head, 2005; Sori et al., 2014). However, inferring past climate from layer properties (e.g., reflectance and protrusion) remains uncertain.

One significant difference between the two poles is the composition of ice at the surface. High-albedo residual ice caps remain at both poles after retreat of the much larger seasonal CO_2 caps. The southern residual ice cap is dominated by a few-meter-thick layer of CO_2 ice (Kieffer, 1979; Thomas et al., 2000). The northern residual ice cap (NRC) is composed of water ice, is on the order of a meter thick (Herkenhoff et al., 2007), Study of the NRC can inform us of the potential link between climate and polar geology. The NRC directly participates in the current climate by supplying the majority of atmospheric water vapor, globally, in northern summer (Smith, 2008). Past residual caps (now layers within the NPLD) were also likely to have interacted and therefore been influenced by past climates. Finding similarities between the features of ice within the PLD and ice comprising the NRC could identify a past climate similar to today's. We are interested in the physical properties (density, potential layering, etc.) of the NRC and their geographic variability so that we can better understand how ice properties reflect the conditions of formation. Understanding the current climate and NRC can potentially unlock a larger climate record. Additionally, knowing the physical properties are important for designing a future landed mission.

Several studies have analyzed NRC albedo and composition (e.g., Kieffer, 1990; Langevin et al., 2005), yet comparably few have addressed its thermophysical state (Paige et al., 1994; Putzig et al., 2005), and none has addressed how these properties change with depth. The present-day mass balance of the NRC is unknown (Byrne, 2009). Langevin et al. (2005), using near-infrared spectral measurements, concluded that the surface of the NRC is coarse-grained ice, implying net ablation and the exposure of older ice. The same study also found the surface to be mostly dust free, which is unexpected for a sublimating layer, where formation of a surface lag seems likely. Brown et al. (2016), also using near-infrared spectral measurements, observed transitions between accumulation and ablation as a function of season but did not favor a particular net mass balance. Smith et al. (2016), using sounding radar, reported a packet of ice-rich layers (on the order of hundreds of meters thick), consistent with a recent period of accumulation, although this evidence cannot be used to invoke accumulation today. Impact craters on the NRC imply craters with tens of meters of relief are removed in tens of thousands of years, although crater interiors may be preferential sites of ice deposition (Banks et al., 2010; Landis et al., 2016).

Knowledge of how density varies with depth constrains environmental conditions (e.g., ice accumulation rates) that are vital to understanding how the climate affects polar stratigraphy. In terrestrial ice sheets and glaciers, the density of ice increases with depth; that is, ice deposited at the surface, typically as highly porous snow (>50% porosity), undergoes densification and will evolve toward low-porosity glacial ice. The primary physical mechanisms involved in near-surface terrestrial densification are gravity-driven compaction and temperature-gradient driven vapor transport (Arthern & Wingham, 1998; Herron & Langway, 1980).

Adapting terrestrial models of ice densification to Mars, Arthern et al. (2000) found that this process should occur more slowly under the drier, lower-gravity Martian conditions. Unlike Earth, densification on Mars is dominated by vapor transport through the pore space in the ice. The predicted depth-density profiles of Martian ice are especially sensitive to the accumulation rate. If accumulation rates are low, zero-porosity ice will be present at the surface. When accumulation rates are sufficiently high, low densities can be maintained at the surface (e.g., 360 kg/m^3 or ~60% porosity).

The focus of this study is the physical nature of the NRC or what we consider the most recent and potentially active layer of the NPLD. Constraining the thermophysical properties of today's NRC can inform us how NPLD layers form and the vertical structure of the NRC can provide insight into the recent climate. Here we investigate how relevant properties of NRC water ice (e.g., density and albedo) vary, both laterally across the NRC and vertically into the subsurface.

Observed temperatures of Mars have been used previously to constrain thermophysical parameters of the near surface (Kieffer et al., 1977; Paige et al., 1994; Putzig et al., 2005). It is common to use thermal inertia (TI; expressed in units J m^{-2} K^{-1} s$^{-1/2}$) to describe thermophysical properties.

$$\mathbf{TI} = \sqrt{k\rho c} \tag{1}$$

Here k is the thermal conductivity (W m^{-1} K^{-1}), ρ is the bulk density (kg/m^3), and c is the specific heat capacity (J kg^{-1} K^{-1}). Surface temperatures are affected by a region of the subsurface approximated by the thermal skin depth, δ, in meters.

$$\delta = \frac{TI}{\rho c} \sqrt{\frac{P}{\pi}} \qquad (2)$$

Here P is the period of a sinusoidal surface temperature variation (e.g., approximately diurnal or seasonal) in seconds. This relationship between TI and skin depth assumes a homogeneous subsurface (i.e., constant thermal properties with depth). For the properties of zero-porosity ice, and the period of one Martian year, the thermal skin depth is 6.4 m. If we assume a situation with an ice porosity of 50% (assuming properties described in section 3.2.2), we find a skin depth of 4.4 m. The depth of sensitivity varies with a number of factors (e.g., latitude or magnitude of seasonality, subsurface layering, and seasonal CO_2 frost properties) and therefore cannot be defined by a single depth.

Investigators have previously explored the thermal nature of the NRC with thermal-infrared data sets (Paige et al., 1994; Putzig et al., 2014; Putzig & Mellon, 2007). Paige et al. (1994) used Viking Infrared Thermal Mapper (IRTM) observations to derive albedo and thermal inertia simultaneously (similar to this study). They characterized the NRC as a high-albedo (>0.40), high-TI unit (>750 J m^{-2} K^{-1} s$^{-1/2}$), in contrast to the surrounding, lower-TI regolith. Paige et al. (1994) also show that the presence of thin (approximately millimeters) coatings of dust are consistent with IRTM observations. Putzig and Mellon (2007) prescribe albedo in their fitting approach, retrieve a TI value for each temperature measurement, and average the results. However, near-surface layering (Bandfield & Feldman, 2008; Putzig et al., 2014) results in a seasonally dependent "apparent" TI that is difficult to compare to that derived from temperature measurements acquired over a significant portion of the Martian year (e.g., from Paige et al., 1994, and this work). Regardless, their averaged TI is consistent with the NRC as a high-TI unit. In section 4.1, the results of our work will be compared to these earlier studies, where applicable.

Earlier studies have used thermal models with depth-dependent properties for Mars (Bandfield, 2007; Bandfield & Feldman, 2008; Mellon et al., 2004; Putzig et al., 2014; Putzig & Mellon, 2007) and the Moon (Hayne et al., 2017; Vasavada et al., 2012), to explore surfaces where changes with depth are expected. We explore three relationships of depth versus density (i.e., abrupt, linear, and exponential changes in ice density) in order to compare the near-surface structure of the NRC with predicted profiles (e.g., Arthern et al., 2000).

2. Methods

2.1. Observational Data

Data used in this study were acquired by the Thermal Emission Spectrometer (TES) aboard Mars Global Surveyor (MGS). MGS was operational over four Mars years (MY), specifically MY24–MY28 (see Piqueux et al., 2015, for a description of the Martian calendar). The primary science orbit of MGS was inclined approximately 93°, which resulted in high data density near the Martian poles (Figure 1), useful for a study of polar surface properties. Unfortunately, it also results in a region of low-to-zero data density poleward of 87°N. This near-polar region was only observed sporadically via cross-track spacecraft rolls and off-nadir pointing of TES. Because data are sparse here, we ignore this region.

TES consists of a thermal-infrared spectrometer as well as coaligned visible and thermal-infrared bolometers. A single TES footprint is approximately 3 × 3 km but is lengthened by a factor of 2–3 in the along-track direction due to smearing (Christensen et al., 2001; Putzig et al., 2005; Titus et al., 2001). We assume brightness temperatures derived from the thermal infrared bolometer represent kinetic surface temperatures, similar to previous studies that used TES data to interpret thermophysical properties (Putzig et al., 2005; Putzig & Mellon, 2007). We include observations poleward of 70°N, for all Mars years, and restrict emission angles to ≤20°. Additionally, data with "bad" nadir optical depth ratings are omitted (Christensen et al., 2001). However, optical depth retrievals are sparse over the NRC due to relatively low daytime peak surface temperatures (i.e., <220 K), which are insufficient for spectrometer retrievals (Smith et al., 2001). Because erroneous data are still possible over the cap we ignore brightness temperatures <160 and >350 K. A temperature of 160 K is roughly 10 K higher than the expected kinetic temperature of CO_2 ice on Mars and is chosen due to the likely heterogeneous defrosting of CO_2-covered terrain within a TES pixel (Bapst et al., 2015; Piqueux et al., 2015). Thus, this step removes TES observations over surfaces, even those partially bearing seasonal CO_2 frost, from our study.
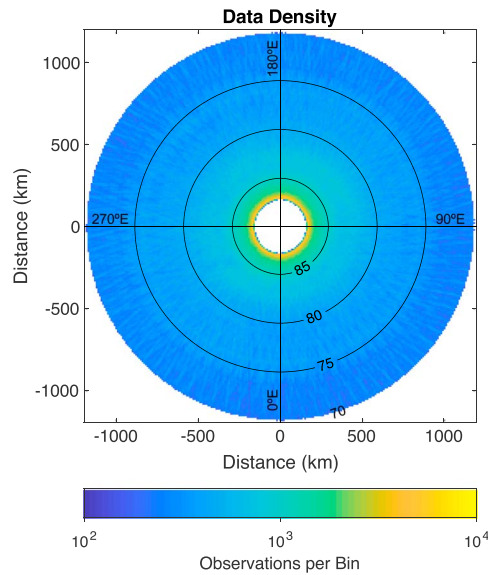
Figure 1. Number of observations per 10×10 km bin in azimuthal equidistant projection centered at the north pole with longitude and latitude labeled. Note the logarithmic scale and the increase in density toward the pole.

The latitudes of TES observations are converted to distance from the pole via the MATLAB Mapping Toolbox "distance" function, which uses a Martian reference ellipsoid and returns the arc length between two points on the ellipsoid surface (here the observation and the pole). The data are then divided into 10×10 km bins. Data and results are presented in an azimuthal equidistant projection centered at the north pole. Data above 70°N are display where 0°E longitude is at the bottom of each figure, increasing counterclockwise (see Figure 1 for geographic coordinate labels). Bins with fewer than 100 observations are omitted from the results presented.

Model Description and Fitting Procedures

A 1-D thermal diffusion model is employed to generate surface temperatures in order to link the measured surface temperatures to near-surface thermophysical properties. The model boundaries are controlled by insolation/emission at the surface, with conduction of heat into the subsurface, and geothermal heat (30 mW/m^2; Davies & Arvidson, 1981) at the base. Model simulations are carried out for a range of input parameters (Table 1) where the parameter space was iterated on and selected based on the range of derived results. For simplicity, we assume a constant elevation of $-3,000$ m to calculate CO_2 condensation temperatures, from rescaling the Viking Lander pressure measurements (Tillman et al., 1993) using an atmospheric scale height of 10.8 km. Atmospherically scattered visible light is parameterized as an additional 2% of the solar flux, while downwelling infrared is an additional 4% of the noontime flux (Aharonson & Schorghofer, 2006; Kieffer et al., 1977; Schorghofer & Edgett, 2006). Cases without atmospheric radiation were tested and had negligible impact on the derived results, with the greatest difference observed in albedo. We refer the reader to Bapst et al. (2018) for additional description of the thermal model.

In all cases the thermophysical properties of surface materials are those of water ice of varying density. Layers of regolith at the surface are not investigated or expected over the NRC due to its high albedo (Figure 2) and previous thermophysical analysis (Paige et al., 1994). At zero porosity (solid ice) we assume thermal properties of $k = 3.2$ W m^{-1} K^{-1}, $\rho = 920$ kg/m^3, and $c = 1,600$ J kg^{-1} K^{-1}. For porous ice, density scales linearly with porosity, c remains constant, and k follows an empirical relationship based on the measured thermal conductivity-density relationship of terrestrial snowpack (described below; Calonne et al., 2011). Hemispheric or bond albedo is derived as part of the model solution and emissivity is prescribed as 1.0 except when CO_2 ice is present, where the emissivity lowers to 0.85 and albedo is fixed at 0.65. These properties were validated by comparing model output to GRS derived CO_2 thicknesses (Kelly et al., 2006).

How thermal conductivity changes with ice porosity is of major relevance to this work. We adopt an expression of thermal conductivity as a function of ice density (equation (3)) from a study on terrestrial

Table 1
Lookup-Table Elements

Parameter	Range
Latitude	70°–90° in 0.5° increments
Albedo	0.05–0.5 in 0.025 increments
Surface porosity	0–0.95 in 0.05 increments
	(equivalent to thermal inertia range of ~50–2,200 J m^{-2} K^{-1} s$^{-1/2}$)
Abrupt transition to zero-porosity ice	Depths of 0.01, 0.025, 0.05, 0.1, 0.2, 0.3, 0.4, 0.5, 0.6, 0.7, 0.8, 0.9, 1, 1.5, 2, 2.5, 3, 3.5, 4, and 5 m
Exponentially decreasing porosity	*e*-folding depths of 0.05, 0.1, 0.2, 0.3, 0.4, 0.5, 0.6, 0.7, 0.8, 0.9, 1, 1.25, 1.5, 2, 2.5, 3, 3.5, 4, 4.5, and 5 m
Linearly decreasing porosity	Porosity gradient of 0.01, 0.02, 0.03, 0.04, 0.05, 0.06, 0.07, 0.08, 0.09, 0.1, 0.2, 0.3, 0.4, 0.5, 0.6, 0.7, 0.8, 0.9, 1, and 2 m^{-1}
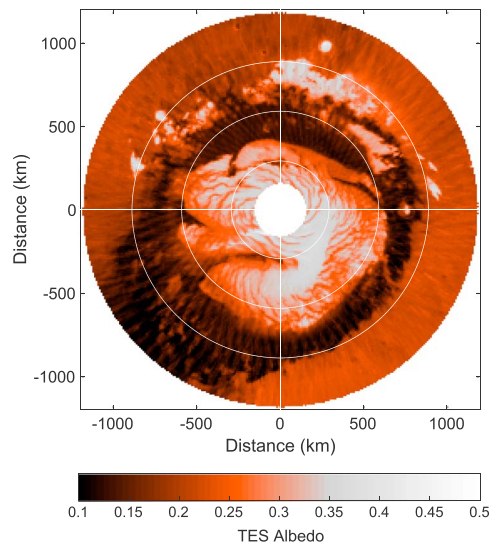
Figure 2. Mean Thermal Emission Spectrometer (TES) Lambert albedo poleward of 70°N in 10 × 10 km bins, including only data between $L_S = 100°$–150°.

snowpack (Calonne et al., 2011). We modify this expression to match the conductivity of pure water ice at Martian temperatures (i.e., $k = 3.2$ W m^{-1} K^{-1} or TI = 2,200 J m^{-2} K^{-1} s$^{-1/2}$ for zero porosity) by applying a constant scaling factor of ~1.6 (not included in equation (3)).

$$k = 2.5 \times 10^{-6} \rho^2 - 1.23 \times 10^{-4} \rho + 0.024 \tag{3}$$

Different models of thermal conductivity versus density (Figure 3) as well as the temperature-dependent effects on thermal properties are explored in section 4.3 but do not largely affect the results or conclusions presented using the model of Calonne et al. (2011). There remains considerable uncertainty in the microstructure of water ice and its effect on thermal conductivity under Martian conditions (Siegler et al., 2012), which differ from theoretical predictions (e.g., Mellon et al., 1997). Previous studies have also focused largely on pore-filling ice within regolith, and not snowpack evolution, hence the adoption of empirical models from terrestrial studies.

The simplest subsurface model investigated here is the vertically homogeneous case (i.e., constant thermal properties with depth) that has been used in previous derivations of thermal properties of the north polar region (Paige et al., 1994; Putzig et al., 2005). Porosity and albedo are free parameters in this case.

Three separate depth-density relationships are explored beyond the homogeneous case, introducing a third free parameter (Figure 4). The parameter ranges explored in each case are shown in Table 1. The three cases are as follows:

1. Linearly increasing density with depth until solid ice is reached. This best resembles profiles of depth and density present in Arthern et al. (2000).
2. Exponentially increasing density with depth that approaches solid ice (Hayne et al., 2017).
3. An abrupt increase in density to that of solid ice at a discrete depth (akin to a solid ice table, e.g., Mellon et al., 2009; Schorghofer, 2010).

For our fitting metric, we calculate the root-mean-square (RMS) temperature difference between TES-derived and model surface temperatures. The minimum RMS value calculated across our modeled parameter space (Table 1) qualifies as our best fit. All valid data points within a bin are included in calculating RMS temperature, as opposed to the "one-point" method where albedo is prescribed (e.g., Putzig et al., 2005; Putzig & Mellon, 2007). As a single temperature measurement in time is nonunique (e.g., due to the time of day, layering, or uncertainty in surface albedo), multiple temperatures must be used to constrain vertically heterogeneous thermal properties and surface albedo. Each binned temperature time series (~10^2–10^3 data points; see Figure 1) is tested against ~6,800 independent models for cases with depth-dependent properties.

The work presented here omits data acquired within specific seasons. We find it is especially important to omit spring data ($L_S = 0°$–90°) as during this time the seasonal layer of CO_2 ice is sublimating at the surface (Piqueux, Kleinböhl, et al., 2015). We adopt a seasonal window after CO_2 ice has defrosted. TES albedo time series suggest seasonal defrosting occurs until $L_S \sim 110°$, which we use as the start of our window. Pilorget et al. (2013) document the thermal effect of lithic material that is jettisoned from beneath sublimating slabs of CO_2 at the south pole during spring, leading to appreciable thicknesses of nonicy material (millimeters) deposited on the surface. This can result in temperatures above that of CO_2 condensation. This process is may be present in the north as evidenced in TES temperature data (Figure 5). Our 1-D thermal model can only represent the surface as either CO_2 covered or not, whereas in reality the defrosting process may be heterogeneous at scales below TES's spatial resolution (as is true for regolith at the Phoenix Lander site; Searls et al., 2010). Thus, during spring, TES measurements may contain a mix of temperatures from CO_2-covered, CO_2-free, and dust-covered CO_2 surfaces, resulting in erroneous fits between our model and the observations (Figure 5). This further complicates
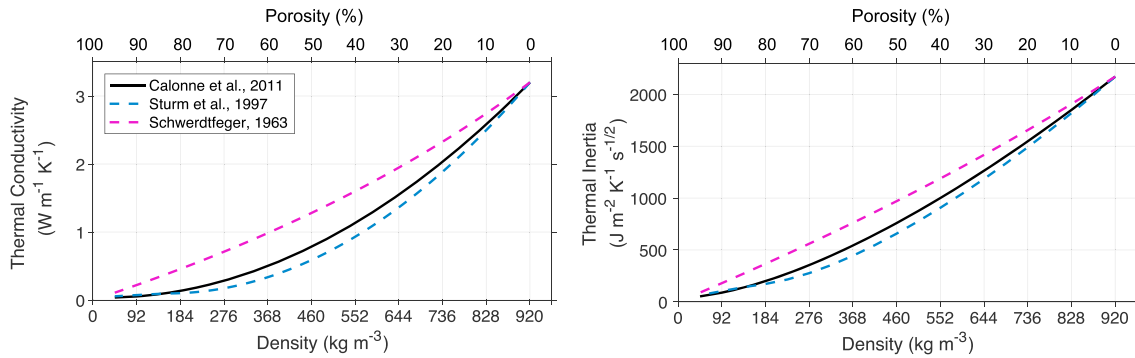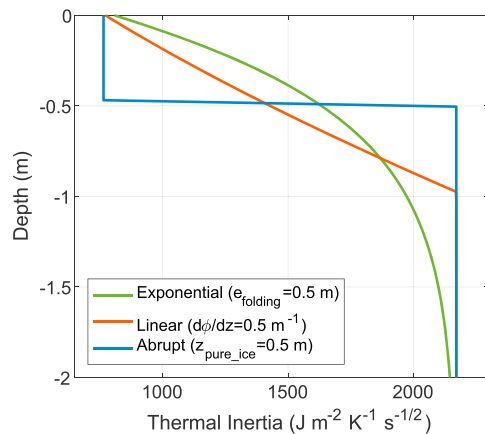
Figure 3. Relationships explored in this work between (left) ice conductivity and (right) thermal inertia, as a function of density/porosity of ice.

determining a precise date for fitting that is void of seasonal frost. We explored fitting with other seasonal windows starting at different times, that is, $L_S = 0°–180°$. Differences in derived best fits using a seasonal window starting between $L_S = 100°–150°$ were small, with our preferred choice of $L_S = 110°$ as this is around the earliest date of complete defrosting at the highest latitudes explored. The choice of end season also made little difference as long as the window extends over the onset of seasonal CO_2 ice since we omit temperatures <160 K ($L_S \sim 180°$).

Quantifying the uncertainty in derived best fit properties is problematic due to unknowns that could affect temperatures measured by TES (e.g., emission and absorption by atmospheric aerosols). These effects dominate other contributions such as instrument noise, which introduces relatively small amounts of uncertainty on derived temperature (Christensen et al., 2001). The bottom row of Figure 5 shows calculated RMS temperature differences and outlines the general range surrounding best fit properties. In the homogeneous case, derived surface albedo is more constrained than porosity. For relatively high TI (i.e., low porosity) materials studied in this work, the range of high-quality fits for porosity is relatively large due to the limited spread in temperatures of high TI materials. For example, in Figure 5 an RMS temperature of ~4 K could be met for ice of zero porosity or ice of 40% porosity. For the homogeneous solutions the reader should ignore small changes in TI across regions that exhibit large values of derived TI (e.g., >1,500 J m^{-2} K^{-1} s$^{-1/2}$).

When considering depth-dependent models (Figure 5, bottom right), acceptable solutions can be met for a number of surface porosity and depth-dependent TI combinations (e.g., 70% surface porosity and 0.05-m depth to zero-porosity ice or 40% surface porosity and 0.2-m depth to zero-porosity ice, etc.). The reader should not focus on one combination (e.g., the reported best fit) but instead consider the improvement in RMS fit (section 3.3) as to whether there is evidence of near-surface layering and understand there is a range of acceptable layering combinations in surface porosity and depth-dependent space.


Figure 4. Example of depth-density relationships explored in this work. Each model displayed has a surface porosity of 50% (equivalent TI = 760 J m^{-2} K^{-1} s$^{-1/2}$) and densifies toward zero porosity, that is, slab ice where TI = 2,200 J m^{-2} K^{-1} s$^{-1/2}$. TI = thermal inertia.

3. Results

Model fits of albedo and near-surface thermal properties are presented in this section. Because our model is designed to retrieve the thermal properties of water ice with varying porosity, our results over regolith-covered surfaces are not valid for depth-dependent cases. For this reason, bins that share derived surface TI < 1,100 J m^{-2} K^{-1} s$^{-1/2}$ in the homogeneous case are masked in the plots of depth-dependent cases.

3.1. Homogeneous Case

Derived TI in the homogeneous case is typically high (>1,000 J m^{-2} K^{-1} s$^{-1/2}$) across the NRC and its icy outliers (i.e., lower-latitude residual ice that is discontinuous from the NRC; Figure 6). Model-derived albedo of
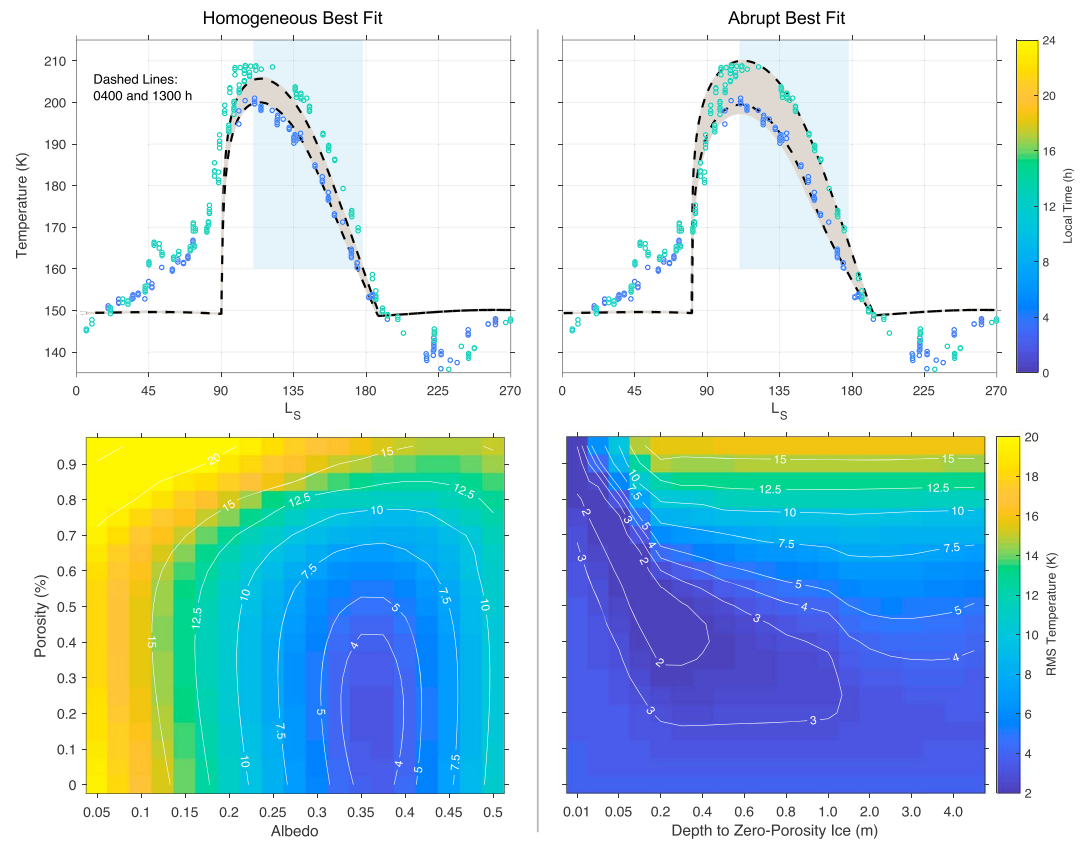
Figure 5. The top row shows TES temperatures for a single 10×10 km bin located in Gemina Lingula at 81.4°N, 9.6°E and is colorized by local time, with our fitting window depicted by the blue shaded region. In addition to TES data, our 0400 and 1300 hr best fit models are shown for two cases where grey shading indicates the diurnal range: (top left) homogeneous or no depth dependence and (top right) abrupt change to zero-porosity ice. Best fit RMS temperatures are 3.3 and 1.2 K, respectively. The derived best fit properties for the homogeneous case were a porosity of 20% and albedo of 0.375. For the abrupt case the derived properties are a surface porosity of 70%, albedo of 0.35, and a depth to zero-porosity ice of 0.05 m. The bottom row shows derived RMS temperatures against our fitting parameters where (bottom left) is our homogeneous case and (bottom right) is the abrupt case but is shown for only our best fit albedo. TES = thermal emission spectrometer; RMS = root-mean-square.

the NRC is consistent with the pattern of observed albedo across the NRC (Figure 2). Limiting our analysis to NRC material with derived albedo ≥0.35 (approximately three thousand 100-km^2 bins), yields a mean NRC TI of 1,871 J m^{-2} K^{-1} s$^{-1/2}$ and standard deviation of 270 J m^{-2} K^{-1} s$^{-1/2}$. Heightened derived TI (>1,600 J m^{-2} K^{-1} s$^{-1/2}$) is present in general poleward of 85°N, on the edge of the NRC near Olympia Planum and Gemina Scopuli, and among the outliers. On the lower end of the derived TI range is a substantial fraction of Gemina Lingula and Gemina Scopuli (~150–250 km from the southern edge of the mapped NRC) and shows derived TI <1,500 J m^{-2} K^{-1} s$^{-1/2}$. The northern plains surrounding the NRC show derived TI values <600 J m^{-2} K^{-1} s$^{-1/2}$ consistent with a homogeneous fit of ground ice overlain by a thin layer of ice-free regolith (Mellon et al., 2009). This vertical inhomogeneity is reflected in relatively large best fit RMS temperatures.

3.2. Depth-Dependent Cases

The three depth-density relationships explored (i.e., abrupt, exponential, and linear changes in thermal properties with depth; Figure 4) all yield similar best fits for derived values of albedo and surface TI (Figure 7). The derived bond albedo is lower across the NRC and is higher over the outlier units than what was derived in the homogeneous case (<0.05 absolute difference in either case; Figure 6).
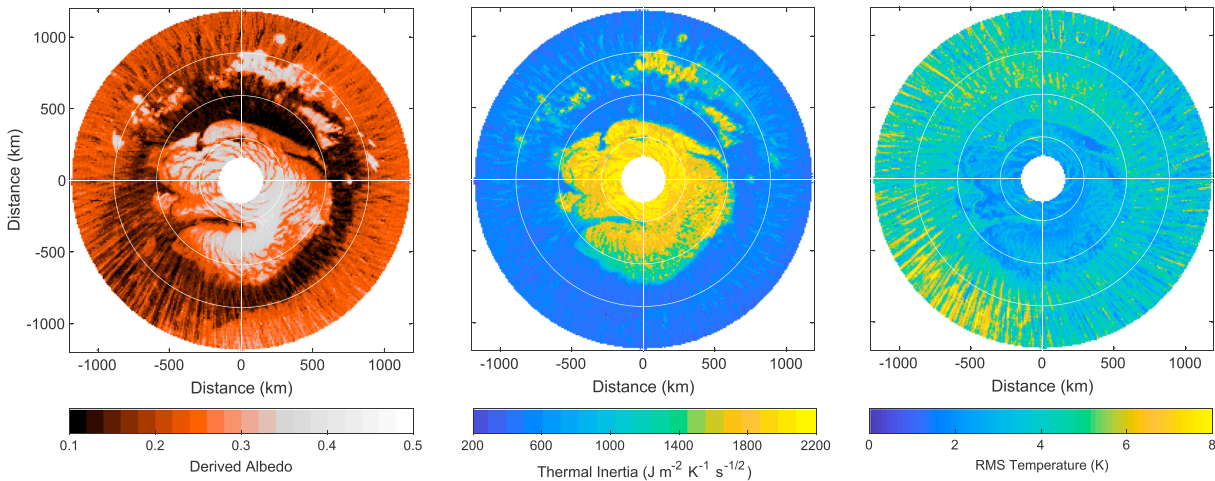
Figure 6. Derived albedo, thermal inertia (TI), and root-mean-square (RMS) temperature for the north polar region of Mars above 70°N for the homogeneous case (i.e., no depth dependency).

There are apparent changes in patterns of surface TI between depth-dependent cases and the homogeneous case. We find that values of surface TI are lower ($<1{,}000$ J m^{-2} K^{-1} s$^{-1/2}$) for almost the entirety of the NRC and its outliers. A delineation in surface TI is apparent between much of the NRC edge and interior ice. The broad regions of low derived surface TI coincide with shallow depth-dependent values, suggesting increases in density <0.5 m in the subsurface (Figure 7). Regions of relatively high surface TI, found at the edge of the NRC and around Chasma Boreale, vary in latitudinal extent from tens of kilometers to hundreds of kilometers. These regions are characterized by their relatively low albedo (<0.3; Figure 2, 6, and 7) and higher surface TI ($>1{,}100$ J m^{-2} K^{-1} s$^{-1/2}$). The icy outliers span a range of surface TI from 400 to 1,200 J m^{-2} K^{-1} s$^{-1/2}$ and are more similar to the low surface TI regions of the NRC interior than its edges in TI and albedo.

Additionally, we explore the best fit depth-dependent relationship for each case (Figure 7, right column). For the abrupt scenario, we display the best fit depth to zero-porosity ice. For linear and exponential cases, we plot the *e*-folding depth of the porosity. We find abrupt and *e*-folding depths correspond to the pattern observed in surface TI. The regions of the NRC where we derive lower surface TI exhibit transitions to solid ice that are shallow, between 0.05 and 0.5 m, while regions with higher surface TI (e.g., NRC edge and west of Chasma Boreale) exhibit greater depths to zero-porosity ice. The shallowest depth-dependent values are observed over Gemina Lingula and the icy outliers. Ultimately, we cannot favor one depth-dependent relationship over another but instead identify regions whose temperatures are consistent with models that include subsurface layering.

3.3. Best Fit Comparison

We compare the best fit RMS temperature of the three depth-dependent cases explored (i.e., abrupt, exponential, and linear) to the homogeneous case (Figure 8). Regolith-dominated surfaces are poorly fit by our thermal models, as expected, and so are masked similar to Figure 7. All models with depth-dependent properties show a near-identical improvement over the homogeneous case, and therefore, one cannot be favored over another. The largest improvements in best fit RMS are seen primarily across Gemina Lingula and the icy outliers. The fit did not substantially improve over the southern edge of Gemina Lingula, a region west of Chasma Boreale, and ice present in western Olympia. Lastly, the highest latitudes investigated showed little difference in fit quality, which could be attributed to the lack of diurnal temperature variations, which are essential in constraining layered cases (as opposed to seasonal temperature variations that constrain bulk TI).

3.4. Properties of Residual Ice

To further explore the vertical structure of the ice of the NRC, we chose three regions of interest in an attempt to cover the range of surface TI derived over the cap (Figures 7 and 8). We selected a 10×10 bin area ($\sim 10^4$ km^2) in Gemina Lingula (centered at 81.7°N, 5.2°E and relatively low surface TI), a region west of Chasma Boreale (centered at 82.9°N, 305.4°E with intermediate-to-high surface TI), and a sample of residual
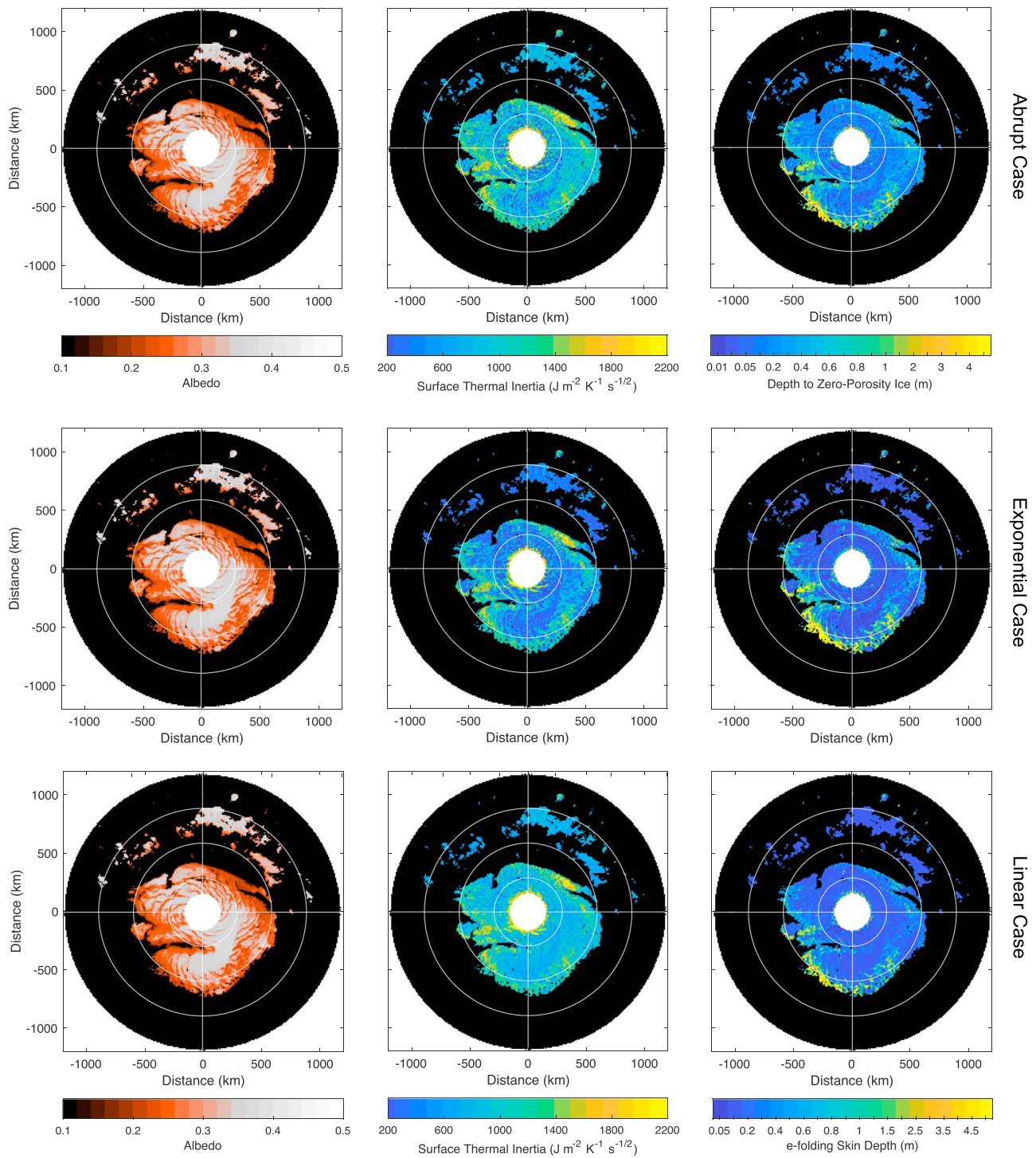
Figure 7. Best fit albedo, surface thermal inertia, and depth-dependence for the three cases explored. Plotted properties have regolith-dominated regions masked out (black). The linear case of depth dependence is expressed as an *e*-folding depth for ease in comparing results to the exponential case.

ice adjacent to the east of the polar erg, Olympia Planum (centered at 83.3°N, 127.9°E). Bins sampled are subject to the same mask as used in Figure 7; that is, bins that have TI <1,100 J m^{-2} K^{-1} s$^{-1/2}$ from the homogeneous fit are not included. Derived surface porosity and depth-dependent properties are shown for each case and depict the general trends in our regions of interest (Figure 9). We primarily report results in terms of porosity which can be converted to thermal conductivity or thermal inertia after section 2.2. (see Figure 3).
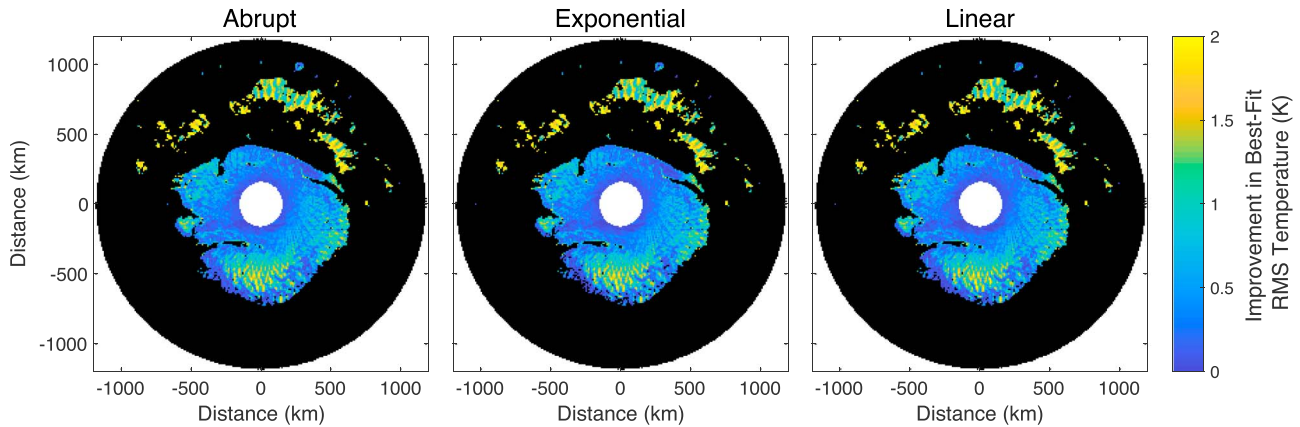
Figure 8. Improvement in best fit root-mean-square temperature for the three cases of depth dependence over the homogeneous case. Green and yellow colors indicate regions where the fit was improved by including depth-dependent properties. Dark blue (approximately zero) indicates no improvement over homogeneous models.

Models with depth-dependent density converge on similar solutions of surface TI and subsurface changes in density (Figures 7 and 9). As stated in section 3.2, for regions of the NRC with low surface TI, we derive relatively shallow depths to zero-porosity ice. Best fits for abrupt transitions to zero-porosity ice are primarily
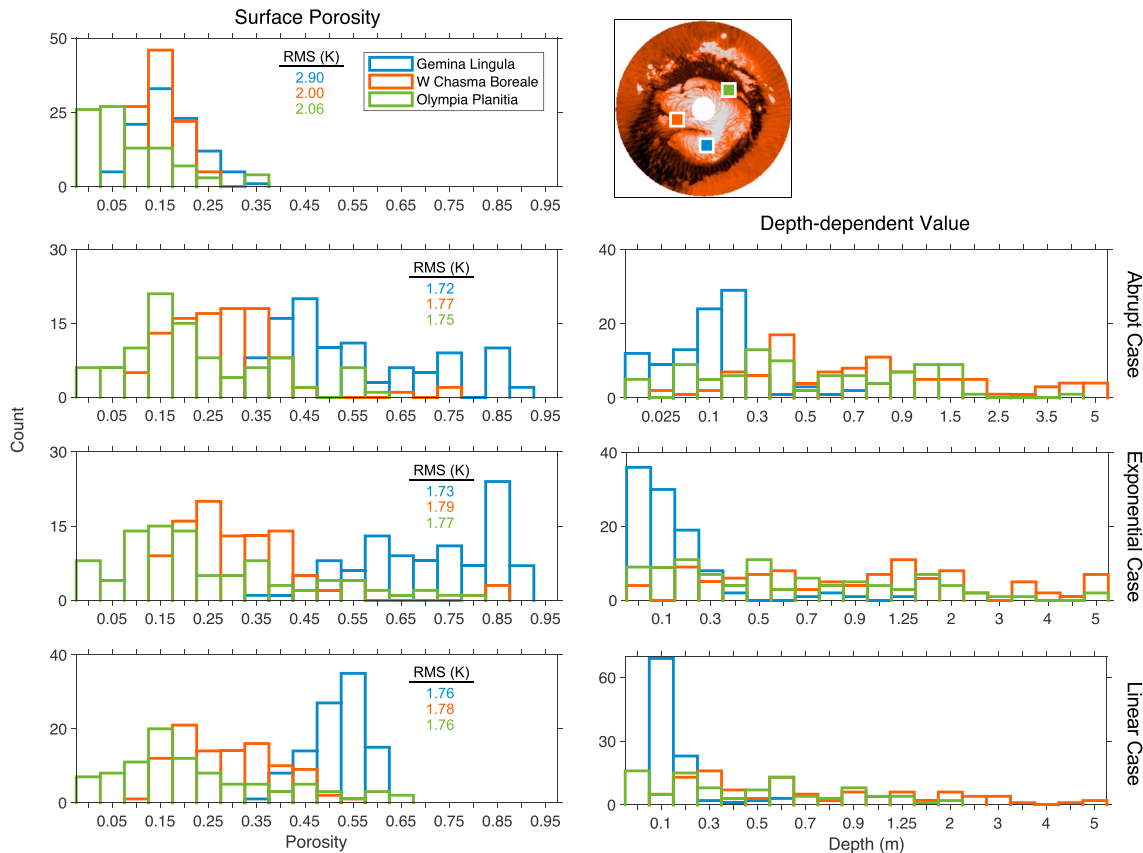
Figure 9. Histograms of derived surface porosity and depth-dependence for a region of Gemina Lingula, the region west of Chasma Boreale, and Olympia. Also displayed are the mean root-mean-square (RMS) temperature differences for each region and case. Regions of low surface thermal inertia (e.g., Gemina Lingula) correspond to shallower depth to zero-porosity ice, for depth-dependent cases. Note that the horizontal axis of depth-dependent properties for the abrupt case does not match the others due to different lookup table elements (Table 1).
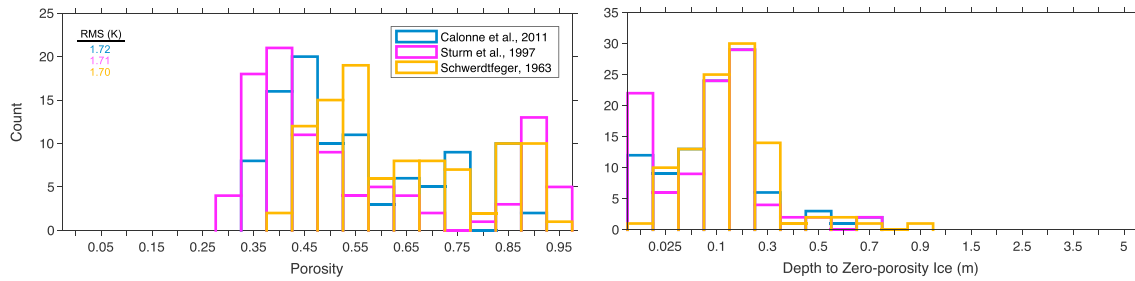
Figure 10. Histograms of derived surface porosity and depth to zero-porosity ice (abrupt change with depth) for the three models of ice conductivity explored (see Figure 3). The sampled region is the same area of Gemina Lingula described in section 3.4 and Figure 9. Also displayed is the mean root-mean-square (RMS) temperature difference for each model tested. In the depth to zero-porosity ice histogram all three models share the same two most common values at 0.1 and 0.2 m.

<0.3 m over Gemina Lingula. Other low-surface-TI regions, which includes much of the NRC and the icy outliers, have similar depths to zero-porosity ice (Figure 7).

Ice Conductivity Models and Temperature Dependence

The relationship between the density of water ice in the NRC and its conductivity is uncertain for a number of reasons, many relating to the microstructure of the ice (e.g., pore radius, grain size, and degree of round-ness; see Sturm et al., 1997). Because we lack **in situ** measurements of these properties on Mars, we explore, in addition to the model by Calonne et al. (2011), two additional models for ice conductivity: Sturm et al. (1997) and Schwerdtfeger, 1963; see Figure 3). The models tested do not result in appreciable differences in derived properties (Figure 10). Thus, our results and interpretations are not particularly sensitive to alternative models of thermal conductivity for porous water ice.

The temperature-dependent effects on ice thermal properties are well known and used in terrestrial glaciology (Cuffey & Paterson, 2010; Yen, 1981). Here we consider the effect of temperature on thermal conductivity, k, and heat capacity, c, after Cuffey and Paterson (2010).

$$c = 152.5 + 7.122T \tag{4}$$

$$k = 9.828 \ \exp\left(-5.7{\times}10^{-3}T\right) \tag{5}$$

Uncertainty in ice microstructure will have a major impact as these properties are valid for only zero-porosity water ice. The addition of porosity and interstitial gases of varying composition, density, and temperature (e.g., the Martian atmosphere) into the pore space can significantly change the effective conductivity (Mellon et al., 1997; Sturm et al., 1997). Here we determine how the temperature-dependence of the solid conductivity and heat capacity affect our results. The conductivity is again modified to be consistent with values used previously. Additionally, because the temperature-dependent model is computationally slower, only a single bin is tested and is the same location within Gemina Lingula as referenced in Figure 5.

Table 2
Effect of Temperature-Dependent Properties on Derived Parameters

Derived property	Homogeneous case		Abrupt case	
	Temperature independent	Temperature dependent	Temperature independent	Temperature dependent
Surface porosity	0.2	0.2	0.7	0.45
Albedo	0.375	0.35	0.35	0.325
Depth to zero-porosity ice (m)	N/A	N/A	0.05	0.2
RMS temperature (K)	3.3	3.1	1.2	1.2

Note. RMS = root-mean-square; N/A = not applicable.
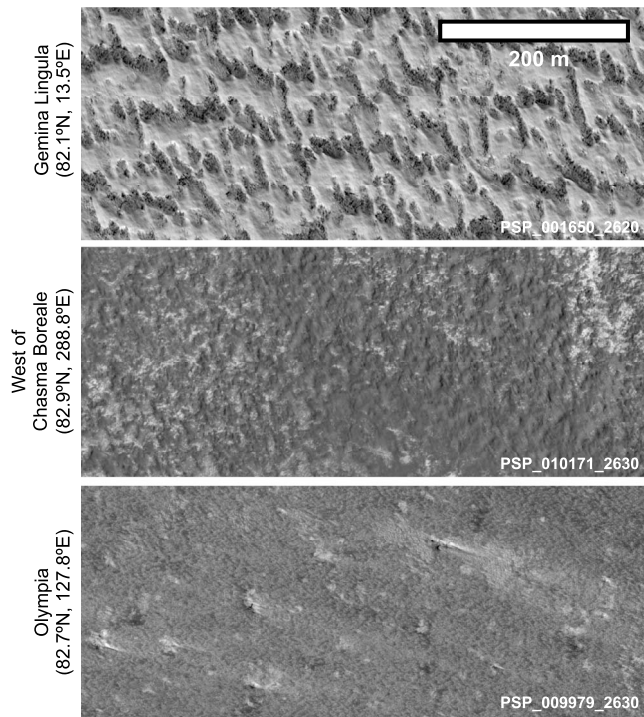
Figure 11. Samples from High Resolution Imaging Science Experiment (HiRISE) images over our three regions of interest from section 3.4. Gemina Lingula exhibited low surface thermal inertia (TI), regions west of Chasma Boreale yield intermediate-to-high surface TI, and Olympia, which yields the highest derived TI. HiRISE image IDs (from top to bottom) are PSP_001650_2620, PSP_010171_2630, and PSP_009979_2630.

In all cases the best fit RMS temperature is consistent when using both temperature-independent and temperature-dependent properties (Table 2). The derived properties are in close agreement for the homogeneous case with only a small change in derived albedo. In the case of depth-dependent models, the difference is more pronounced. We argue, as is depicted in Figure 5, that the difference between best fits is negligible for a range of surface porosity and depth-dependent combinations. Because there is little difference in our RMS temperature between these cases, they are equally plausible but do support near-surface (<0.5 m) layering as they provide a substantially better fit over the homogeneous model.

4. Discussion and Conclusions

4.1. Comparison to Previous Work

Our findings for the homogeneous case (section 3.1) are greater than TI derivations made by previous authors using Viking IRTM data. Paige and Ingersoll (1985) derived a TI poleward of 86°N of $1,250 \pm 400$ J m^{-2} K^{-1} s$^{-1/2}$ using an energy balance approach and Viking data. Using Viking IRTM-derived surface temperatures Paige et al. (1994) found an average TI of 1,151 J m^{-2} K^{-1} s$^{-1/2}$ poleward of 86°N. We lack TES observations poleward of 87°N, due to the orbital inclination of MGS; however, we have ~10^3 TI derivations above 86°N, which yield a mean value of 2,038 J m^{-2} K^{-1} s$^{-1/2}$, and a standard deviation of 136 J m^{-2} K^{-1} s$^{-1/2}$. Under the assumption of a homogeneous subsurface, differences between derived TI and that of previous authors are substantial. This could be due to a variety of factors. One is the seasonal range where we fit data. Paige et al. (1994) investigated data acquired between $L_S \sim 90°–120°$. TES data are available at all seasons, and we selected the range of $L_S \sim 110°–180°$. We defend our exclusion of early northern summer ($L_S = 90°–110°$) as there is evidence from TES albedo that seasonal frost is still sublimating during this period (potentially water frost at the latest dates). Our models also have different treatment for atmospheric radiation, where we employ a simple scheme after Schorghofer and Edgett (2006). Paige et al. use a no-atmosphere scheme for their primary results but do investigate a number of atmospheric scenarios using a more sophisticated radiative transfer model and find the effect on derived properties to be significant (and often result in an increase in the apparent TI derived). IRTM data are acquired at higher emission angles compared to TES due to the orbital inclination of the Viking orbiters (~40°; Snyder, 1977) and are thus more susceptible to atmospheric effects (TES data are predominantly ~0° emission angle). The spiral troughs are partially resolved in our analysis (affecting only overlapping or neighboring bins) but are mixed with flat-lying residual ice in IRTM data, which could affect derived thermal properties. Lastly, the local time coverage of Viking IRTM is superior to that of TES, which primarily acquired data at ~0200 and ~1400 hr. However, TES does capture near-maximum and near-minimum temperatures of the diurnal curve (see Figure 5). We are fitting both diurnal and seasonal aspects of the data, and so our results represent the best fit to both.

Putzig and Mellon (2007) used a one-point method for TI derivation that is susceptible to error at polar latitudes. Despite these differences, detailed below, the surface TI derived by Putzig and Mellon (2007) over the NRC is consistent with our results, albeit with substantial scatter. One known effect the one-point method can introduce for a nonhomogeneous subsurface is a seasonally dependent TI (Bandfield, 2007; Bandfield & Feldman, 2008; Putzig et al., 2014) and are thus averaged in the retrievals of Putzig and Mellon (2007). Putzig et al. (2014) study the effect of layering on derived TI in polar dunes in Olympia Planum; however, we are not aware of any thermal study applying this method to the NRC. Lastly, Putzig and Mellon (2007) do not omit springtime data, and so potentially erroneous TI derivations are averaged into their polar results.

4.2. Spatial Heterogeneity of the North Residual Cap

The results of our fitting show that the majority of the NRC is consistent with depth-dependent or layered models, although the style of layering cannot be deduced from analysis (Figures 7 and 8). The strongest evidence for layering is found where the fits improved most, that is, over Gemina Lingula and the icy outliers. This result is not entirely unexpected given the layered nature of the NPLD as exposed in polar troughs as well as the vertically inhomogeneous nature of terrestrial ice deposits. The geographic diversity in the near-surface layering suggests that mechanisms that control the physical properties of residual ice (e.g., accumulation or ablation) are spatially diverse. Interpreting derived properties in these terms is important for understanding mass balance across the NRC and its evolution.

We interpret the derived properties of low surface TI regions of the NRC as the consequence of recent ice accumulation, where the material being deposited at the surface is relatively porous (>40%) and densifies with depth (Figure 9). The relatively high albedo of these regions is also consistent with recent accumulation. Along the edge of the NRC and the region west of Chasma Boreale, we derive denser ice (<40% surface porosity) along with relatively low surface albedo (Figures 7 and 9).

Densified ice might be present near the surface for several reasons. One possible explanation is that the ice is accumulating slowly, and therefore, low-porosity ice cannot be maintained against densification near or at the surface (Arthern et al., 2000). Although high-TI regions mostly exhibit lower albedo (i.e., the opposite of what one would assume for an accumulating surface), this could be explained by the presence of coarse-grained ice, consistent with ice metamorphism and thus densification. Alternatively, denser ice may be the product of recent ablation. In this scenario, older ice is being exhumed and is retreating, with some mechanism (e.g., eolian transport; Smith et al., 2013) acting to remove lithic material that would otherwise form a lag at the surface. Even with the removal of a potential lag, the surface may include small mixing fractions of dust, consistent with Langevin et al. (2005), and would result in the relatively low surface albedo (Kieffer, 1990; Warren, 1982). We are unable to distinguish between these scenarios with thermal data alone.

The notion that ice at the surface can be simultaneously accumulating and retreating, as a function of location on the NRC, can complicate the interpretation of NPLD layers. It may also help explain the higher density of NPLD troughs and unconformities (Tanaka, 2005) at lower latitudes. Troughs, which are tied to sublimation and eolian processes (Smith & Holt, 2010; Smith et al., 2013), may be aided in initiation due to increased dust content at surface (i.e., lithic material liberated via sublimation of retreating ice).

One particular region of the residual cap edge shows some of the highest derived TI, located at approximately 83°N, 125°E in the Olympia region. Unlike the previously mentioned high-TI examples, this region also appears to have an anomalously high TI in the homogeneous solution. All cases yield low surface porosities of ~15% or TI ~ 1,700 J m^{-2} K^{-1} s$^{-1/2}$. This region also exhibits large derived e-folding/abrupt depths, converging on a mostly homogeneous subsurface. Derived albedo is relatively low, likely due to contamination by dust at the surface, but again could be due to coarse-grained water ice. This high-TI signal remains intact in our derivations suggesting that any surface dust layer is of insufficient thickness to act as an effective thermal insulator. We interpret this region of the NRC as composed of older ice than other examples around the NRC edge and favor recent exhumation by simultaneous retreat and removal of lithic material via wind.

The NRC has been imaged at high spatial resolutions and can be compared to our derived surface properties. We use data from the High Resolution Imaging Science Experiment (HiRISE) with up to 25-cm/pixel spatial resolution (McEwen et al., 2007). We focus on the regions of interest outlined in section 3.4, as they span a range of derived surface TI (Figure 11). The surface morphology can vary within a HiRISE image, and our regions of interest span 10^3–10^4 km^2, so Figure 11 is only a sample of these regions.

The sample from Gemina Lingula shows a softened surface texture in the more reflective regions. This softened terrain lies between arrays of dark-toned pits that are regularly spaced by 10–30 m. The higher albedo material may represent porous ice that has accumulated recently, resulting in the low surface TI derived in this region. The region west of Chasma Boreale has considerable diversity as seen by HiRISE, as it is nearby Crotone impact crater and intersects with the sand-rich basal unit (Tanaka et al., 2008). The example from Olympia also exposes basal unit material and is where we derived some of the highest TI in this study, however there is sparse coverage by HiRISE. The terrain is mostly featureless, punctuated by knobby, blocky

structures ~10 m in size that appear to be actively eroding as evidenced by light-toned streaks of material downwind their location. This is consistent with our interpretation of old, and less reflective ice (due to dust) being the product of exhumation and resulting in relatively low derived albedo and high derived TI.

5. Conclusions

In the work presented, we investigated the thermophysical nature of the upper most layer of the NPLD, the NRC, with emphasis on depth-density relationships within the subsurface (depths of decimeters to meters). We find depth dependencies associated within specific regions of the NRC and the icy outliers (i.e., a more porous layer of ice overlying a denser layer). This trend is consistent with the accumulation of ice that then densifies with age and depth as it is buried, as occurs on Earth. The vast majority of these changes in density occur within 0.5 m of the surface.

Results in the region surrounding Chasma Boreale, as well as the edges of the NRC in general, support a more homogeneous subsurface that is denser, and likely older, ice. We interpret ice along the margin of the NRC as having undergone recent ablation or is ablating at present day, which is consistent with its observed low albedo. Our results point to nonuniform accumulation across the residual cap. This is consistent with previous investigations of the uppermost layers of the NPLD, which show evidence for lateral variations in accumulation rates at the present (Tyler & Barnes, 2014) as well as in the past (Becerra et al., 2016).

References

Aharonson, O., & Schorghofer, N. (2006). Subsurface ice on Mars with rough topography. *Journal of Geophysical Research*, *111*, E11007. https://doi.org/10.1029/2005JE002636

Arthern, R. J., Winebrenner, D. P., & Waddington, E. D. (2000). Densification of water ice deposits on the residual north polar cap of Mars. *Icarus*, *144*(2), 367–381. https://doi.org/10.1006/icar.1999.6308

Arthern, R. J., & Wingham, D. J. (1998). The natural fluctuations of firn densification and their effect on the geodetic determination of ice sheet mass balance. *Climatic Change*, *40*(3–4), 605–624. https://doi.org/10.1023/A:1005320713306

Bandfield, J. L. (2007). High-resolution subsurface water-ice distributions on Mars. *Nature*, *447*(7140), 64–67. https://doi.org/10.1038/nature05781

Bandfield, J. L., & Feldman, W. C. (2008). Martian high latitude permafrost depth and surface cover thermal inertia distributions. *Journal of Geophysical Research*, *113*, E08001. https://doi.org/10.1029/2007JE003007

Banks, M. E., Byrne, S., Galla, K., McEwen, A. S., Bray, V. J., Dundas, C. M., et al. (2010). Crater population and resurfacing of the Martian north polar layered deposits. *Journal of Geophysical Research*, *115*, E08006. https://doi.org/10.1029/2009JE003523

Bapst, J., Bandfield, J. L., & Wood, S. E. (2015). Hemispheric asymmetry in Martian seasonal surface water ice from MGS TES. *Icarus*, *260*, 396–408. https://doi.org/10.1016/j.icarus.2015.07.025

Bapst, J., Byrne, S., & Brown, A. J. (2018). On the icy edge at Louth and Korolev craters. *Icarus*, *308*, 15–26. https://doi.org/10.1016/j.icarus.2017.10.004

Becerra, P., Byrne, S., Sori, M. M., Sutton, S., & Herkenhoff, K. E. (2016). Stratigraphy of the north polar layered deposits of Mars from high-resolution topography. *Journal of Geophysical Research: Planets*, *121*, 1445–1471. https://doi.org/10.1002/2015JE004992

Brown, A. J., Calvin, W. M., Becerra, P., & Byrne, S. (2016). Martian north polar cap summer water cycle. *Icarus*, *277*, 401–415. https://doi.org/10.1016/j.icarus.2016.05.007

Byrne, S. (2009). The polar deposits of Mars. *Annual Review of Earth and Planetary Sciences*, *37*(1), 535–560. https://doi.org/10.1146/annurev.earth.031208.100101

Calonne, N., Flin, F., Morin, S., Lesaffre, B., Du Roscoat, S. R., & Geindreau, C. (2011). Numerical and experimental investigations of the effective thermal conductivity of snow. *Geophysical Research Letters*, *38*, L23501. https://doi.org/10.1029/2011GL049234

Christensen, P. R., Bandfield, J. L., Hamilton, V. E., Ruff, S. W., Kieffer, H. H., Titus, T. N., et al. (2001). Mars Global Surveyor Thermal Emission Spectrometer experiment: Investigation description and surface science results. *Journal of Geophysical Research*, *106*(E10), 23823–23871. https://doi.org/10.1029/2000JE001370

Cuffey, K. M., & Paterson, W. S. B. (2010). *Physics of glaciers* (4th ed.p. 693). New York: Elsevier.

Davies, G. F., & Arvidson, R. E. (1981). Martian thermal history, core segregation, and tectonics. *Icarus*, *45*(2), 339–346. https://doi.org/10.1016/0019-1035(81)90039-7

Greve, R., Grieger, B., & Stenzel, O. J. (2010). MAIC-2, a latitudinal model for the Martian surface temperature, atmospheric water transport and surface glaciation. *Planetary and Space Science*, *58*(6), 931–940. https://doi.org/10.1016/j.pss.2010.03.002

Hayne, P. O., Bandfield, J. L., Siegler, M. A., Vasavada, A. R., Ghent, R. R., Williams, J.-P., et al. (2017). Global Regolith Thermophysical Properties of the Moon From the Diviner Lunar Radiometer Experiment. *Journal of Geophysical Research: Planets.*, *122*, 2371–2400. https://doi.org/10.1002/2017JE005387

Herkenhoff, K. E., Byrne, S., Russell, P. S., Fishbaugh, K. E., & McEwen, A. S. (2007). Meter-scale morphology of the north polar region of Mars. *Science*, *317*(5845), 1711–1715. https://doi.org/10.1126/science.1143544

Herkenhoff, K. E., & Plaut, J. J. (2000). Surface ages and resurfacing rates of the polar layered deposits on Mars. *Icarus*, *144*(2), 243–253. https://doi.org/10.1006/ICAR.1999.6287

Herron, M. M., & Langway, C. C. (1980). Firn densification: An empirical model. *Journal of Glaciology*, *25*(93), 373–385. https://doi.org/10.3189/S0022143000015239

Hvidberg, C. S., Fishbaugh, K. E., Winstrup, M., Svensson, A., Byrne, S., & Herkenhoff, K. E. (2012). Reading the climate record of the Martian polar layered deposits. *Icarus*, *221*(1), 405–419. https://doi.org/10.1016/j.icarus.2012.08.009

Kelly, N. J., Boynton, W. V., Kerry, K., Hamara, D., Janes, D., Reedy, R. C., et al. (2006). Seasonal polar carbon dioxide frost on Mars: CO2mass and columnar thickness distribution. *Journal of Geophysical Research*, *112*, E03S07. https://doi.org/10.1029/2006JE002678

Kieffer, H. H. (1979). Mars south polar spring and summer temperatures: A residual CO2frost. *Journal of Geophysical Research*, *84*(B14), 8263. https://doi.org/10.1029/JB084iB14p08263

Kieffer, H. H. (1990). H₂O grain size and the amount of dust in Mars' Residual north polar cap. *Journal of Geophysical Research*, *95*(B2), 1481. https://doi.org/10.1029/JB095iB02p01481

Kieffer, H. H., Martin, T. Z., Peterfreund, A. R., Jakosky, B. M., Miner, E. D., & Palluconi, F. D. (1977). Thermal and albedo mapping of Mars during the Viking primary mission. *Journal of Geophysical Research*, *82*(28), 4249–4291. https://doi.org/10.1029/JS082i028p04249

Landis, M. E., Byrne, S., Daubar, I. J., Herkenhoff, K. E., & Dundas, C. M. (2016). A revised surface age for the North Polar Layered Deposits of Mars. *Geophysical Research Letters*, *43*, 3060–3068. https://doi.org/10.1002/2016GL068434

Langevin, Y., Poulet, F., Bibring, J. P., Schmitt, B., Douté, S., & Gondet, B. (2005). Summer evolution of the north polar cap of Mars as observed by OMEGA/Mars express. *Science*, *307*(5715), 1581–1584. https://doi.org/10.1126/science.1109438

Laskar, J., Correia, A. C. M., Gastineau, M., Joutel, F., Levrard, B., & Robutel, P. (2004). Long term evolution and chaotic diffusion of the insolation quantities of Mars. *Icarus*, *170*(2), 343–364. https://doi.org/10.1016/j.icarus.2004.04.005

Laskar, J., Levrard, B., & Mustard, J. F. (2002). Orbital forcing of the Martian polar layered deposits. *Nature*, *419*(6905), 375–377. https://doi.org/10.1038/nature01066

Levrard, B., Forget, F., Montmessin, F., & Laskar, J. (2007). Recent formation and evolution of northern Martian polar layered deposits as inferred from a Global Climate Model. *Journal of Geophysical Research*, *112*, E06012. https://doi.org/10.1029/2006JE002772

McEwen, A. S., Eliason, E. M., Bergstrom, J. W., Bridges, N. T., Hansen, C. J., Delamere, W. A., et al. (2007). Mars reconnaissance orbiter's high resolution imaging science experiment (HiRISE). *Journal of Geophysical Research*, *112*, E05S02. https://doi.org/10.1029/2005JE002605

Mellon, M. T., Arvidson, R. E., Sizemore, H. G., Searls, M. L., Blaney, D. L., Cull, S., et al. (2009). Ground ice at the Phoenix landing site: Stability state and origin. *Journal of Geophysical Research*, *114*, E00E07. https://doi.org/10.1029/2009JE003417

Mellon, M. T., Feldman, W. C., & Prettyman, T. H. (2004). The presence and stability of ground ice in the southern hemisphere of Mars. *Icarus*, *169*(2), 324–340. https://doi.org/10.1016/j.icarus.2003.10.022

Mellon, M. T., Jakosky, B. M., & Postawko, S. E. (1997). The persistence of equatorial ground ice on Mars. *Journal of Geophysical Research*, *102*(E8), 19,357.

Milkovich, S. M., & Head, J. W. (2005). North polar cap of Mars: Polar layered deposit characterization and identification of a fundamental climate signal. *Journal of Geophysical Research*, *110*, E01005. https://doi.org/10.1029/2004JE002349

Paige, D. A., Bachman, J. E., & Keegan, K. D. (1994). Thermal and albedo mapping of the polar regions of Mars using Viking thermal mapper observations: 1. North polar region. *Journal of Geophysical Research*, *99*(E12), 25959. https://doi.org/10.1029/93JE03428

Paige, D. A., & Ingersoll, A. P. (1985). Annual heat balance of Martian polar caps: Viking observations. *Science*, *228*(4704), 1160–1168. https://doi.org/10.1126/science.228.4704.1160

Phillips, R. J., Zuber, M. T., Smrekar, S. E., Mellon, M. T., Head, J. W., Tanaka, K. L., et al. (2008). Mars north polar deposits: stratigraphy, age, and geodynamical response. *Science*, *320*(5880), 1182–1185. https://doi.org/10.1126/science.1157546

Pilorget, C., Edwards, C. S., Ehlmann, B. L., Forget, F., & Millour, E. (2013). Material ejection by the cold jets and temperature evolution of the south seasonal polar cap of Mars from THEMIS/CRISM observations and implications for surface properties. *Journal of Geophysical Research: Planets*, *118*, 2520–2536. https://doi.org/10.1002/2013JE004513

Piqueux, S., Byrne, S., Kieffer, H. H., Titus, T. N., & Hansen, C. J. (2015). Enumeration of Mars years and seasons since the beginning of telescopic exploration. *Icarus*, *251*, 332–338. https://doi.org/10.1016/j.icarus.2014.12.014

Piqueux, S., Kleinböhl, A., Hayne, P. O., Kass, D. M., Schofield, J. T., & McCleese, D. J. (2015). Variability of the Martian seasonal CO_2 cap extent over eight Mars Years. *Icarus*, *251*, 164–180. https://doi.org/10.1016/j.icarus.2014.10.045

Plaut, J. J., Picardi, G., Safaeinili, A., Ivanov, A. B., Milkovich, S. M., Cicchetti, A., et al. (2007). Subsurface radar sounding of the south polar layered deposits of Mars. *Science*, *316*(5821), 92–95. https://doi.org/10.1126/science.1139672

Putzig, N. E., & Mellon, M. T. (2007). Apparent thermal inertia and the surface heterogeneity of Mars. *Icarus*, *191*(1), 68–94. https://doi.org/10.1016/j.icarus.2007.05.013

Putzig, N. E., Mellon, M. T., Herkenhoff, K. E., Phillips, R. J., Davis, B. J., Ewer, K. J., & Bowers, L. M. (2014). Thermal behavior and ice-table depth within the north polar erg of Mars. *Icarus*, *230*, 64–76. https://doi.org/10.1016/j.icarus.2013.07.010

Putzig, N. E., Mellon, M. T., Kretke, K. A., & Arvidson, R. E. (2005). Global thermal inertia and surface properties of Mars from the MGS mapping mission. *Icarus*, *173*(2), 325–341. https://doi.org/10.1016/j.icarus.2004.08.017

Schorghofer, N. (2010). Fast numerical method for growth and retreat of subsurface ice on Mars. *Icarus*, *208*(2), 598–607. https://doi.org/10.1016/j.icarus.2010.03.022

Schorghofer, N., & Edgett, K. S. (2006). Seasonal surface frost at low latitudes on Mars. *Icarus*, *180*(2), 321–334. https://doi.org/10.1016/j.icarus.2005.08.022

Schwerdtfeger, P. (1963). Measurement of conducted flow of heat in a sea ice cover. *Nature*. Nature Publishing Group, *200*(4908), 769. https://doi.org/10.1038/200769a0

Searls, M. L., Mellon, M. T., Cull, S., Hansen, C. J., & Sizemore, H. G. (2010). Seasonal defrosting of the Phoenix landing site. *Journal of Geophysical Research*, *115*, E00E24. https://doi.org/10.1029/2009JE003438

Siegler, M., Aharonson, O., Carey, E., Choukroun, M., Hudson, T., Schorghofer, N., & Xu, S. (2012). Measurements of thermal properties of icy Mars regolith analogs. *Journal of Geophysical Research*, *117*. https://doi.org/10.1029/2011JE003938

Smith, I. B., & Holt, J. W. (2010). Onset and migration of spiral troughs on Mars revealed by orbital radar. *Nature*, *465*(7297), 450–453. https://doi.org.10.1038/nature09049

Smith, I. B., Holt, J. W., Spiga, A., Howard, A. D., & Parker, G. (2013). The spiral troughs of Mars as cyclic steps. *Journal of Geophysical Research: Planets*, *118*, 1835–1857. https://doi.org/10.1002/jgre.20142

Smith, I. B., Putzig, N. E., Holt, J. W., & Phillips, R. J. (2016). An ice age recorded in the polar deposits of Mars. *Science*, *352*(6289), 1075–1078. https://doi.org/10.1126/science.aad6968

Smith, M. D. (2008). Spacecraft observations of the Martian atmosphere. *Annual Review of Earth and Planetary Sciences*, *36*(1), 191–219. https://doi.org/10.1146/annurev.earth.36.031207.124334

Smith, M. D., Pearl, J. C., Conrath, B. J., & Christensen, P. R. (2001). One Martian year of atmospheric observations by the Thermal Emission Spectrometer. *Geophysical Research Letters*, *28*(22), 4263–4266. https://doi.org/10.1029/2001GL013608

Snyder, C. W. (1977). The missions of the Viking orbiters. *Journal of Geophysical Research*, *82*(28), 3971–3984. https://doi.org/10.1029/JS082i028p03971

Sori, M. M., Perron, J. T., Huybers, P., & Aharonson, O. (2014). A procedure for testing the significance of orbital tuning of the Martian polar layered deposits. *Icarus*, *235*, 136–146. https://doi.org/10.1016/j.icarus.2014.03.009

Sturm, M., Holmgren, J., König, M., & Morris, K. (1997). The thermal conductivity of seasonal snow. *Journal of Glaciology*, *43*(143), 26–41. https://doi.org/10.1017/S0022143000002781

Tanaka, K. L. (2005). Geology and insolation-driven climatic history of Amazonian north polar materials on Mars. *Nature*, *437*(7061), 991–994. https://doi.org/10.1038/nature04065

Tanaka, K. L., Rodriguez, J. A. P., Skinner, J. A., Bourke, M. C., Fortezzo, C. M., Herkenhoff, K. E., et al. (2008). North polar region of Mars: Advances in stratigraphy, structure, and erosional modification. *Icarus*, *196*(2), 318–358. https://doi.org/10.1016/j.icarus.2008.01.021

Thomas, P. C., Malin, M. C., Edgett, K. S., Carr, M. H., Hartmann, W. K., Ingersoll, A. P., et al. (2000). North-south geological differences between the residual polar caps on Mars. *Nature*, *404*(6774), 161–164. https://doi.org/10.1038/35004528

Tillman, J. E., Johnson, N. C., Guttorp, P., & Percival, D. B. (1993). The Martian annual atmospheric pressure cycle: Years without great dust storms. *Journal of Geophysical Research*, *98*(E6), 10963. https://doi.org/10.1029/93je01084

Titus, T. N., Kieffer, H. H., Mullins, K. F., & Christensen, P. R. (2001). TES premapping data: Slab ice and snow flurries in the Martian north polar night. *Journal of Geophysical*, *106*(E10), 23,181–23,196. https://doi.org/10.1029/2000je001284

Tyler, D., & Barnes, J. R. (2014). Atmospheric mesoscale modeling of water and clouds during northern summer on Mars. *Icarus*, *237*, 388–414. https://doi.org/10.1016/j.icarus.2014.04.020

Vasavada, A. R., Bandfield, J. L., Greenhagen, B. T., Hayne, P. O., Siegler, M. A., Williams, J. P., & Paige, D. A. (2012). Lunar equatorial surface temperatures and regolith properties from the Diviner Lunar Radiometer Experiment. *Journal of Geophysical Research*, *117*, E00H18. https://doi.org/10.1029/2011JE003987

Warren, S. G. (1982). Optical properties of snow. *Reviews of Geophysics*, *20*(1), 67. https://doi.org/10.1029/RG020i001p00067

Yen, Y.-C. (1981). Review of thermal properties of snow, ice, and sea ice. CRREL Report 81-10, (81–10), 1–27.